



Effective hydrogenation of g-C₃N₄ for enhanced photocatalytic performance revealed by molecular structure dynamics

Yan Gong^a, Hongkun Li^a, Chen Jiao^b, Qingchi Xu^c, Xiangyu Xu^a, Xiuming Zhang^a, Yufei Liu^d, Ziyang Dai^a, Xiang Yang Liu^{a,c}, Wei Chen^e, Lei Liu^b, Da Zhan^{a,e,*}

^a Research Institute for Soft Matter and Biomimetics, Department of Biomaterials, College of Materials, Xiamen University, Xiamen, Fujian, 361005, China

^b Changchun Institute of Optics, Fine Mechanics and Physics, Chinese Academy of Sciences, Changchun, Jilin, 130000, China

^c College of Physical Science and Technology, Xiamen University, Xiamen, Fujian, 361005, China

^d Key Laboratory of Optoelectronic Technology & Systems (Chongqing University), Ministry of Education, Chongqing, 400044, China

^e Department of Chemistry, National University of Singapore, 3 Science Drive 3, 117543, Singapore



ARTICLE INFO

Keywords:

g-C₃N₄
Hydrogenation
Molecular structure dynamics
Photocatalysis
Charge separation

ABSTRACT

In this work, we report a simple, facile and effective method to simultaneously hydrogenate and exfoliate graphitic-C₃N₄ (g-C₃N₄) through high concentration sulfuric acid treatment. The hydrogenation mechanism of g-C₃N₄ is explained experimentally and it is further revealed in detail by molecular structure dynamics as well as the corresponding electronic structure evolutions. Five different atomic sites in unit cell of g-C₃N₄ are structurally available to be hydrogenated, and four of them are energetically favored to form hydrogenated structures. Different from the pristine g-C₃N₄ that is flat in basal plane, the energetically favored hydrogenation structure of g-C₃N₄ possesses the corrugated fluctuation plane. The hydrogenated g-C₃N₄ structures also present blueshifted UV-vis absorption and photoluminescence (PL) peaks compared to that of pristine g-C₃N₄, and it is well explained by theoretical calculation results that the bandgap becomes larger due to hydrogenation. Finally, it is found that the photocatalytic performance of g-C₃N₄ is dramatically enhanced once the crystal structure is hydrogenated. The enhanced photocatalytic performance is mainly attributed to the hydrogenation caused spatial charge separation due to the redistribution of charge density in both valence band maximum and conduction band minimum. The revealing of spatial charge separation provides insight into the deep understanding of hydrogenation mechanism of g-C₃N₄, which is critically significant for designing light-efficient photocatalysis.

1. Introduction

Photocatalysis is the acceleration of a chemical reaction caused by light-absorption induced electron-hole (e-h) pairs in photocatalysts. Traditionally, the inorganic semiconductor photocatalysts with appropriate bandgaps, such as metal oxides [1] and metal sulfides [2] are good in photocatalytic behavior but normally hindered by noblesse, toxicity and scalability [3]. In recent years, graphitic-C₃N₄ (g-C₃N₄) has been studied intensively in scientific community because it is a metal free photocatalytic material with excellent performances in degrading organic pollution dyes for environmental remediation and splitting water for solar energy harvest applications [4–8]. g-C₃N₄ can be synthesized by a very simple and facile method through thermal polymerization of various earth abundant and inexpensive nitrogen-rich precursors, meaning that the scalability is also available for fulfilling the industry demand in future [9,10]. Normally, the photon excited e-h

pairs in g-C₃N₄ recombine rapidly to illuminate strong light, which is at the expense of decreasing photocatalytic activity. Recently, synthesizing the g-C₃N₄-based hybridized composites to form heterojunctions and direct Z-scheme have been developed for further improving photocatalytic performance, and the main mechanism of both methods is ascribed to effective charge separation spatially between two materials (Fig. 1a,b) [11–15]. Thus, highly active g-C₃N₄-based photocatalysts should be designed on the basis of spatial separation of light excited e-h pairs effectively. Comparing to synthesizing g-C₃N₄-based strongly coupled hybridized composite to form heterojunctions or direct Z-scheme structure, acid treatment of g-C₃N₄ has also been widely applied in enhanced photocatalytic applications due to simple, controllable, metal-free, cheap, and environmental friendly [5,16–22]. However, the understanding of the hydrogenation mechanism from viewpoint of molecular structure dynamics and electronic structure evolution has not been revealed, particularly that the effective spatial separation of

* Corresponding author.

E-mail address: zhanda@xmu.edu.cn (D. Zhan).

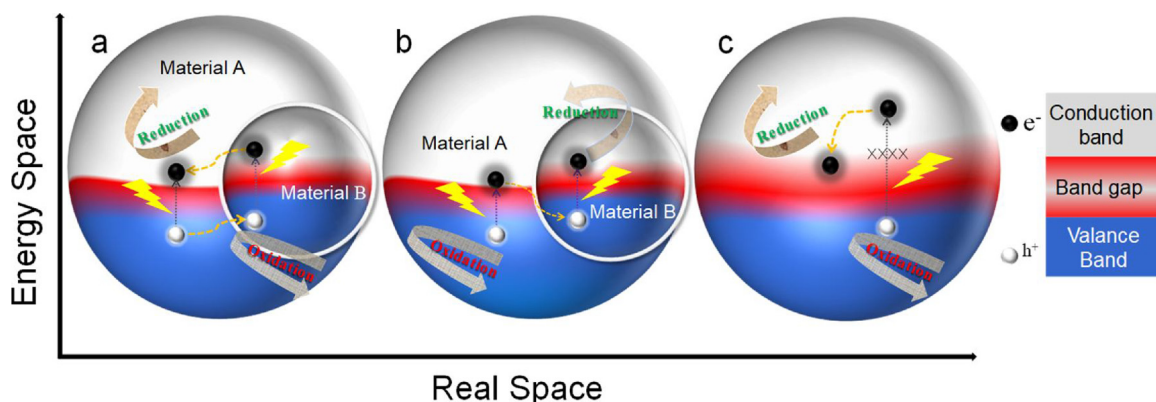


Fig. 1. Schematic illustration of photocatalytic mechanism for two different semiconductor materials hybridized as a composite to form (a) heterojunction and (b) direct Z-scheme; (c) proposed mechanism on the spatial charge separation in an independent system. In this mechanism, the photon excited electrons in deep conduction band cannot relax to the conduction band minimum at the same position in real space because of the charge density absence (denoted by $\times \times \times$). Instead, the electrons in deep conduction band relaxed to the other positions in real space, elongating the lifetime of both electrons in conduction band and holes in valance band for enhanced photocatalytic performance. In these figures, the horizontal axis schematically represents the real space and the vertical axis represents the energy space.

photon induced e-h pairs for enhancing the overall photocatalytic performance has not been reported. In this work, we used dicyandiamide as the precursor to prepare g-C₃N₄. With subsequent sulfuric acid treatment, the bulk g-C₃N₄ suffered hydrogenation and exfoliation effects simultaneously, rendering the exfoliated nanosheets be able to form aqueous suspensions. The theoretical study also revealed in detail that four different types of hydrogenation sites are preferred due to the lower system total energy. The hydrogenated g-C₃N₄ shows remarkably enhanced photodegradation performance because it is found that this independent system possesses redistributed charge densities in both valance band maximum and conduction band minimum, which spatially separates the photon induced e-h pairs (Fig. 1c), and it will be discussed in detail later.

2. Results and discussion

2.1. Characterization of physical properties

As shown in Fig. 2a, the color of as-received g-C₃N₄ is yellow. After hydrogenation treatment in 98% H₂SO₄, the color of g-C₃N₄ mixed in water changed to white. This phenomenon has also been observed by Zhu's group [23]. The morphology structures of the as-received and acid treated g-C₃N₄ samples are characterized by scanning electron microscope (SEM) and transmission electron microscope (TEM) as shown in Fig. 2b-e. It can be seen that after high concentration sulfuric acid treatment, the g-C₃N₄ was undergone an obvious microstructure evolution from dense solid bulk to the fluffy mashed tiny parts (Fig. 2b,c), and the layers become thinner (Fig. 2d,e). The evolution of microstructure after acid treatment shows the direct evidence of exfoliation. In addition to the evolution of microstructure observed by SEM and TEM, the detailed evolution of crystal lattice information, including vibrational modes as well as the interplanar spacing were characterized by Fourier-transform infrared spectroscopy (FTIR) and X-ray diffraction pattern (XRD), respectively. As shown in Fig. 3a, there are many absorption peaks can be observed in both as-received and acid treated g-C₃N₄ in the range between 1200 and 1700 cm⁻¹. The absorption peaks at frequencies of ~1635 and ~1560 cm⁻¹ should be attributed to the stretching modes of C=N; the absorption peaks at ~1400 and ~1343 cm⁻¹ are owing to the stretching modes of aromatic CN heterocycles; the ~1320 and ~1250 cm⁻¹ absorption peaks should be originated from the stretching vibrations of the connected units of N-(C)3 (full condensation) or CNH-C (partial condensation) [17]. Furthermore, the breathing mode of triazine units also shows strong absorption at ~812 cm⁻¹ for both as-received and acid-treated samples.

The observation of above typical stretching vibration modes indicates the existence of heptazine-derived repeating units. It is also noted that the absorption peaks become weaker after acid treatment, inferring the partly breakage of tri-s-triazine units. It should be ascribed to the chemical reaction in the high concentration sulfuric acid to structurally create some defects in rich N-bridged structures as suggested [5,24]. It is noteworthy that these IR modes of the acid-treated sample are actually show slightly shift to lower wavenumbers compared to that of the as-received bulk sample. This phenomenon shows the evidence of hydrogenation and exfoliation as reported elsewhere [17]. It should be noted that no direct evidence to show sulphate related peaks in the acid treated samples, which is similar to other works on sulfuric acid treated g-C₃N₄ [23,25].

The XRD patterns of bulk g-C₃N₄ and the hydrogenated sample are shown in Fig. 3b. The strongest diffraction peak at 27.68° is caused by the characteristic interlayer-stacking of aromatic systems (002), indicating that the interlayer space $d = 0.323$ nm in the bulk g-C₃N₄. The other relatively weak peak at low diffraction angle of 12.98° of bulk g-C₃N₄ is derived from in-planar repeated tri-s-triazine units (100), showing that the repeatable hole to hole distance in the basal plane is 0.65 nm. After sulfuric acid treatment, the crystal structure shows difference remarkably. The reflection peak associated with the c axis repeating unit (002) becomes less pronounced and wider, and it shifts to a higher angle of 27.83°, indicating the less crystalline quality as well as shrinkage of the interplanar distance. The tighter packing of the hydrogenated g-C₃N₄ nanosheets can exclude the intercalation. This phenomenon is usually observed for the distorted basal plane of g-C₃N₄ and can be explained by the strong van der Waals attraction between the adjacent stacked layers [26]. Furthermore, the decrease of the interlayer space is also the evidence to exclude the protonation induced intercalation [23,25]. The original weak peak at 12.98° is disappeared almost. It makes clear that the aromatic systems formed in-plane periodicity has been destroyed strongly. This is probably another evidence to show the sulfuric acid induced hydrogenation effect, which gives rise to the breakage of the bonds as similar effect has been reported elsewhere [27,28]. This is also in accordance with the results concluded by FTIR as aforementioned. Meanwhile, two new sharp peaks at ~12.4° and ~6.2° are observed, and it is also noted that there are some additional sharp peaks appeared in the diffraction angles between 22° and 32° after hydrogenation. This is ascribed to the strong interaction between the basal plane of g-C₃N₄ and sulfuric acid to form hydrogenated structures during the acidification treatment process [25], and the newly appeared peaks have been observed in g-C₃N₄ nanorod which present similar effect in enhancing the photocatalytic performance

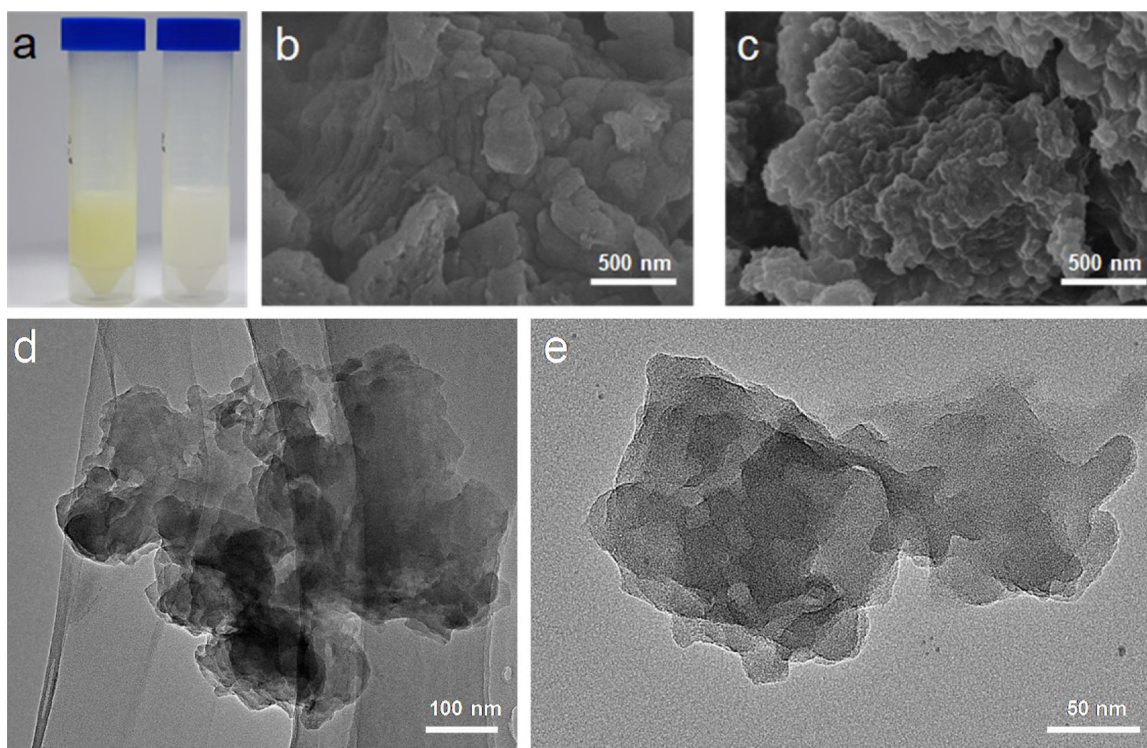


Fig. 2. (a) The photos of as-received $\text{g-C}_3\text{N}_4$ bulk sample (left, yellow) and acid treated $\text{g-C}_3\text{N}_4$ (right, white); SEM images of (b) as-received $\text{g-C}_3\text{N}_4$ sample, and (c) the high concentration sulfuric acid treated $\text{g-C}_3\text{N}_4$; TEM images of (c) as-received $\text{g-C}_3\text{N}_4$ sample, and (d) the high concentration sulfuric acid treated $\text{g-C}_3\text{N}_4$ (For interpretation of the references to colour in this figure legend, the reader is referred to the web version of this article).

[29]. To understand the crystal structure evolution, theoretical calculation in terms of various possible hydrogenation sites has been carried out. As shown in Fig. 4a, from the geometry of crystal structure, the possible hydrogenated sites of $\text{g-C}_3\text{N}_4$ include 2 different C atoms (Fig. 4b,c) and 3 different N atoms (Fig. 4d-f), respectively (The computational detail is given in the Supporting Information). Once the hydrogenation occurs, each of four hydrogenation types (hydrogen respectively bonds to N_{E} , N_{C} , C_1 , C_2) evolved to corrugated structure to break the original flat plane except for hydrogenation of N_{S} , which still keeps basal plane flat. The corrugations of the basal plane explains broadening of XRD main peak (002) as well as causes the other possible diffraction angles due to the newly appeared in-plane periods. Furthermore, as can be seen in Table 1, the hydrogenation of N_{S} site does not decrease the system energy, but on the contrary, the total energy of the system decreases dramatically when the hydrogenation causes the

corrugation of basal plane (N_{E} , N_{C} , C_1 , C_2), indicating that these four types of hydrogenation are energetically favorable. Therefore, the theoretical models of hydrogenation gives rise to the corrugation of basal plane, which explains the broadening of XRD main peak (002) and appearance of new additional peaks very well.

To further investigate the chemical structure and oxidation state of elements C and N, the X-ray photoelectron spectroscopy (XPS) measurement was conducted. As shown in Fig. S1, no evident change in the binding energies of both C and N after acid treatment, indicating the relatively stable chemical inertness of the melon units. However, if we carefully deconvolute the XPS curves, it can be found that after acid treatment, there is an additional peak observed at ~286.3 eV for C1s (Fig. S1a,b), and the intensity portion of peak at ~400.9 eV for N1s increased (Fig. S1c,d). The former one can be probably assigned as C–H bond [30], and the later one has been assigned as C–N–H [31].

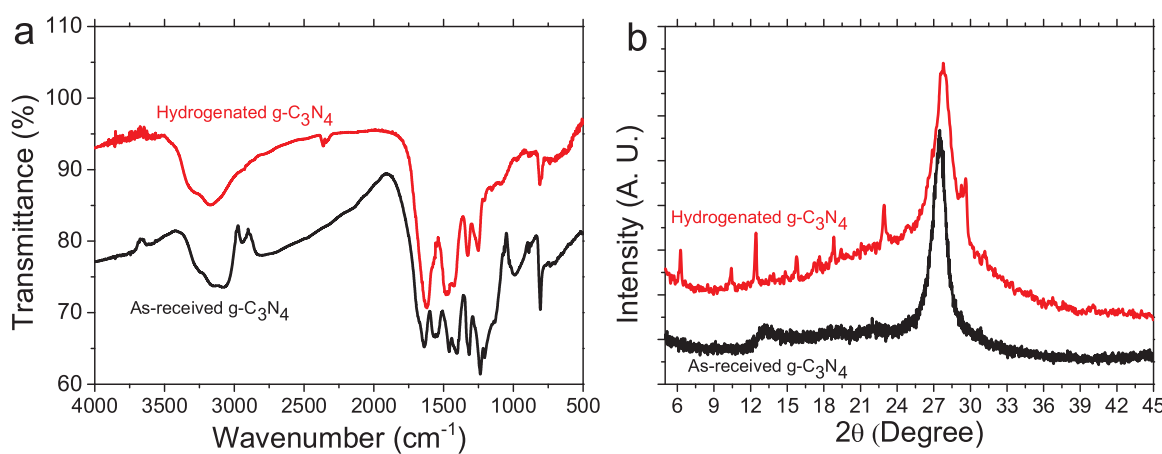


Fig. 3. Investigation of the crystal lattice information of both as-received $\text{g-C}_3\text{N}_4$ bulk sample and hydrogenated $\text{g-C}_3\text{N}_4$ nanosheets. (a) FTIR spectra; (b) XRD patterns.

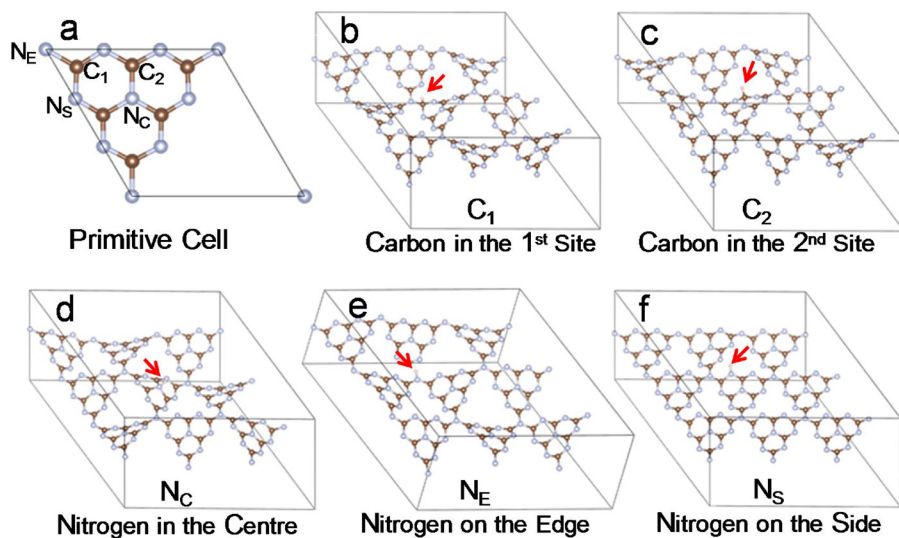


Fig. 4. (a) Relaxed crystal structure of pristine $\text{g-C}_3\text{N}_4$; Different types of hydrogenated $\text{g-C}_3\text{N}_4$ with hydrogenation at (b) carbon in the 1st site (C_1), (c) carbon in the 2nd site (C_2), (d) the center nitrogen atom (N_c), (e) edge nitrogen atom (N_e), and (f) side nitrogen atom (N_s).

Table 1

Energy diagram and lattice parameters of pristine and different types of hydrogenated $\text{g-C}_3\text{N}_4$.

Motif	Total Energy (eV)	a (Å)	b (Å)
C_1	-3.00	20.41	20.42
C_2	-2.51	20.44	20.41
N_c	-2.78	20.42	20.39
N_s	0	20.84	20.84
N_e	-3.29	20.45	20.60
Pristine	0	20.81	20.82

Therefore, the XPS results also support the structure dynamics on the basis of hydrogenation.

In addition to the structure analysis, it is also important to know the effective surface area. Besides using Brunauer–Emmett–Teller (BET) method to approach the value of surface area, the effective surface area extrapolated by electrochemical method through the calculation of C_{dl} is more widely used in catalysis and energy storage, which reflect the real area available for ions or molecules adsorption. Thus, we carried out the electrochemical test to extrapolate the effective surface area, as shown in Fig. S2, the effective surface area of $\text{g-C}_3\text{N}_4$ does not show obvious change after acid treatment.

2.2. Electronic properties

Furthermore, the internal electronic structure evolution is also of particular importance. As $\text{g-C}_3\text{N}_4$ is a direct bandgap semiconductor, thus the light can be absorbed effectively when the excitation photon energy is resonant with the band edge. As UV-vis absorption spectrum is very sensitive to the modified electronic structure, it can be used to probe the electronic structure evolution of $\text{g-C}_3\text{N}_4$. As shown in Fig. 5a, the UV-vis absorption band edge shifts to higher energy after the sulfuric acid treatment. As the sulfuric acid is proton-rich, thus the obvious blueshift of UV-vis absorption peak is probably due to hydrogenation induced interaction with the lone pair electron of the aromatic nitrogen atoms [19,32]. The overall interaction effect gives rise to downshift of Fermi level due to the external hole doping effect and the broadening of the optical bandgap, resulting in the blueshift for both PL and UV-vis absorption peaks (the blueshifted PL will be discussed in detail later). It is also noteworthy that the degree of blueshifted peak positions can be used to evaluate the degree of hydrogenation [17]. Therefore, we can obviously know that the sample is strongly hydrogenated as the

absorption peak position shifts apparently from ~400 to ~330 nm. Furthermore, the exfoliation of the sample from bulk to thin-layer is undergone a quantum confinement effect, resulting in the larger bandgap, which is in consistent with the blueshifted UV-vis absorption peak [27]. The band gap energies of semiconductors can be estimated by Kubelka–Munk transformation based on the formula $(\alpha h\nu)^{1/n} = A(h\nu - E_g)$. Where α is the absorption coefficient, ν is the light frequency, E_g is the band gap energy, A is a constant and n depends on the characteristics of the semiconductor. As $\text{g-C}_3\text{N}_4$ is a direct bandgap semiconductor, the n is $\frac{1}{2}$. Based on the Kubelka–Munk transformation, the derived optical bandgaps in terms of the light absorption spectra are showing in Fig. 5b. It is clearly show that the optical bandgap of bulk sample shifts to larger from ~2.71 eV to ~3.06 eV after hydrogenation. The photoluminescence (PL) spectra excited by a monochromatic UV laser with wavelength of 325 nm is shown in Fig. 5c. The main emission peak of the bulk $\text{g-C}_3\text{N}_4$ locates at ~440 nm, and it blueshifts to ~420 nm after acid treatment. The obvious blueshift of the emission peak is in accordance with the bandgap blueshift as shown in the Fig. 5b. Moreover, the theoretical calculation shows that the bandgap of all the hydrogenated corrugated crystal structures are all enlarged (Fig. S3b–e) compared to that of pristine $\text{g-C}_3\text{N}_4$ (Fig. S3a), though the N_s -based hydrogenated $\text{g-C}_3\text{N}_4$ with flat basal plane does not shift the bandgap (Fig. S3f). It is noted that the theoretical calculated bandgaps of pristine (~2.7 eV) and various hydrogenated $\text{g-C}_3\text{N}_4$ (~3.1 eV for C_1 , C_2 , N_c and N_e) match the experimental values (Fig. 5b) very well. Therefore, the energetically favored hydrogenation motifs not only relax the flat basal plane to corrugation, but also give the evidence to directly support the blueshift of both PL and UV-vis absorption peaks due to the evolutions of corresponding electronic band structures.

Meanwhile, it is noted that the recombination of excited electron-hole pair shows obvious decrease after hydrogenation treatment as reflected by the obviously decreased PL peak intensity. The relatively weaker PL peak intensity for hydrogenated sample is probably attributed to the effective separation of electron-hole pairs to prevent its recombination.

2.3. Photocatalytic properties and mechanism analysis

With the appropriate bandgap to excite electron-hole pairs effectively, the $\text{g-C}_3\text{N}_4$ is able to photocatalytically produce H_2 by water splitting [6,33], removal of hazardous gas [15,34,35], and it can be also used to photodegrade organic pollutants by decomposition of organic

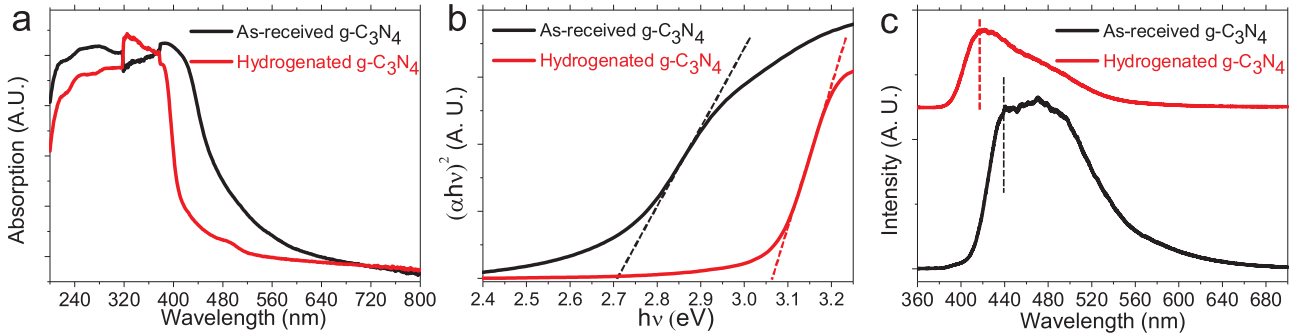
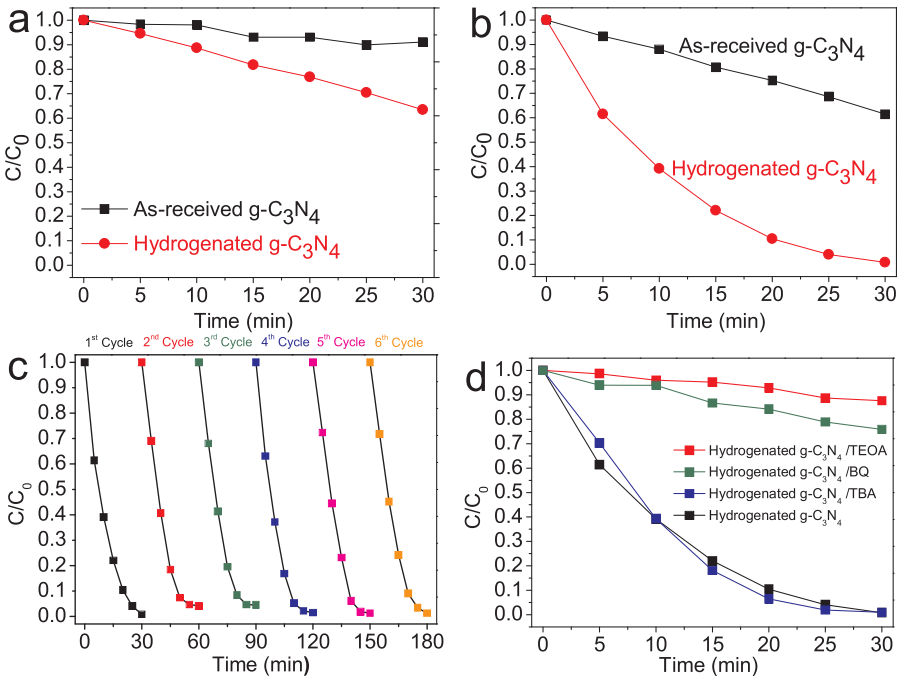


Fig. 5. Internal electronic properties measurement for both as-received g-C₃N₄ bulk sample and hydrogenated g-C₃N₄ nanosheets. (a) UV-vis absorption spectra; (b) the derived optical bandgap spectra. (c) PL spectra.



molecules [36–38]. In this work, the photocatalytic activity of hydrogenated g-C₃N₄ is evaluated by degrading RhB under both visible and UV-vis light, respectively. As shown in Fig. 6a, under visible light irradiation, pristine bulk g-C₃N₄ performs poor photocatalytic activity as only about 10% RhB are degraded after 30 min. After hydrogenation treatment, about 30% RhB dye molecules are degraded after 30 min, showing the enhanced photocatalytic performance. Besides the photodegradation measurement by using visible irradiation, the photodegradation measurement on the basis of using UV-vis irradiation was also conducted. As shown in Fig. 6b, it can be seen clearly that the bulk g-C₃N₄ shows a little bit enhancement in photodegradation of RhB molecules compared to that of visible light irradiation, but the hydrogenated g-C₃N₄ performs much better as the RhB molecules are almost fully degraded in 30 min. This can be understood by two factors which are absorption efficiency and charge separation effect. As the hydrogenation effect shifts the bandgap larger and introduces holes, the relatively lower wavelength (higher energy) photons can be better resonant with the band edge of g-C₃N₄, resulting in light absorption more effective. It is worth noting that the other vital parameters for evaluating the potential practical photocatalysis, such as stability and renewable abilities, have been measured. The hydrogenated g-C₃N₄ performs very good stability in degrading RhB reproducibly, as can be seen in Fig. 6c, the RhB can be fully degraded even after 6 successive cycles (The detailed degradation process reflected by the optical

absorption spectra can be found in Fig. S4). To reveal the active species generated in the photocatalytic degradation process, we introduce certain scavengers, including tert-butylalcohol (TBA, 10%) for hydroxyl radicals (·OH), triethanolamine (TEOA, 10%) for holes (h⁺), and benzoquinone (BQ, 0.5 mM) for superoxide anion radicals (·O₂⁻), respectively. As can be seen in the Fig. 6d, the TBA hardly influenced the photodegradation efficiency; on the other hand, both the TEOA and BQ strongly suppress the photodegradation performance. The results indicate that the h⁺ and ·O₂⁻ are the main species involved in photodegradation process. To further confirm the photocatalytic activity of the hydrogenation effect, the photodegradation of methyl orange (MO) was investigated. It is clear seen in Fig. S5 that the similar enhancement of photocatalytic performance is achieved for hydrogenated sample compared to that of as-received photocatalyst.

Furthermore, it is noted that the recombination of excited electron-hole pair shows obvious decrease after hydrogenation treatment as reflected by the obviously decreased PL intensity. Here, the molecular structure dynamics induced charge redistribution is used to unravel the mechanism for the decreased PL intensity. For pristine g-C₃N₄, the VBM is contributed by p-orbital of N atoms, and the CBM is contributed by p-orbital of both N and C atoms (Fig. S6a, S7a). The charges are distributed uniformly for both VBM and CBM in reciprocal space and they are symmetric in real space. Therefore, the irradiation light excited e-h pairs in energy space (Fig. 7a) are actually not separated in real space

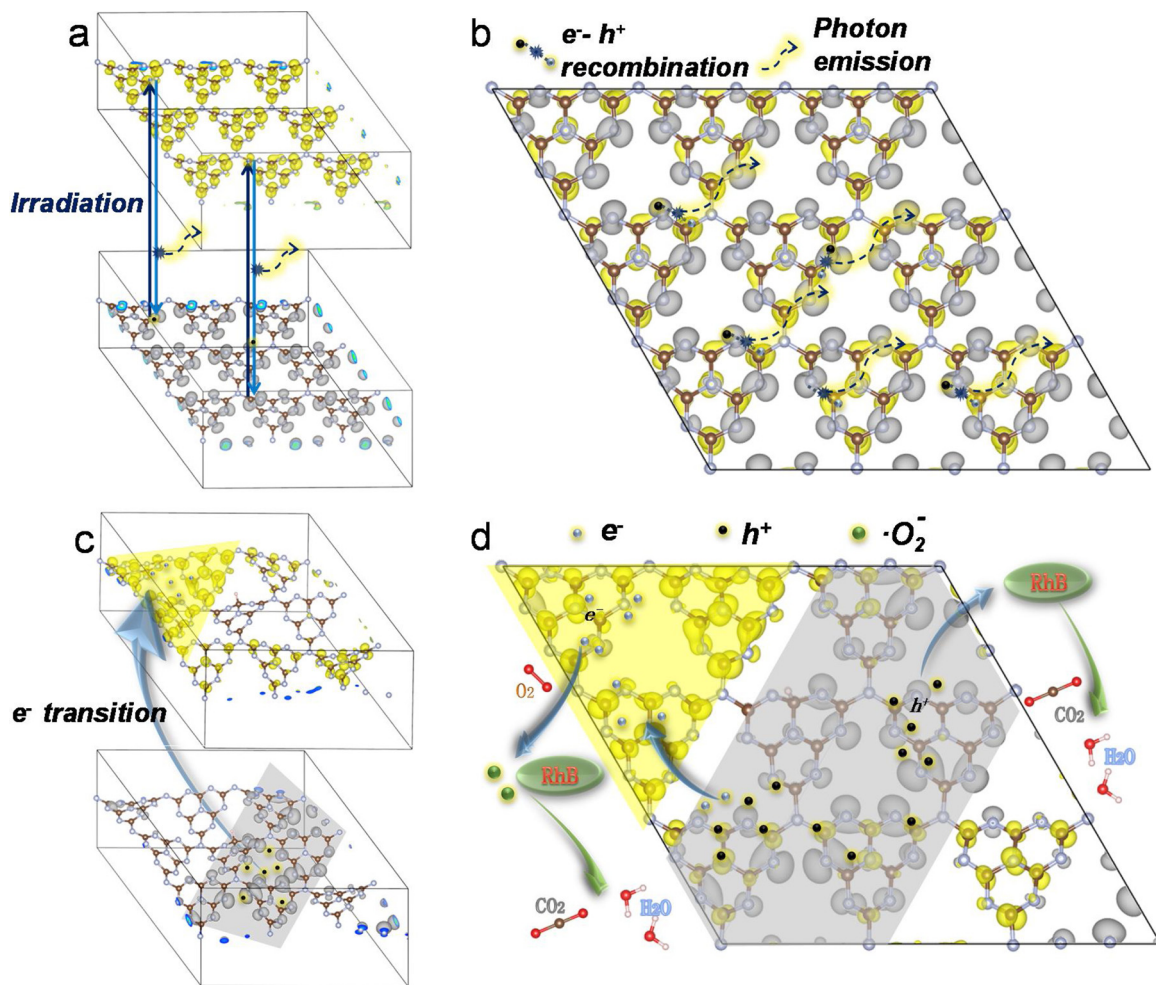


Fig. 7. Schematic illustration of the irradiation light excited e-h pairs and the recombination process. The irradiation photons excite the spatially localized e-h pairs from VBM to CBM and followed by e-h recombination induced photon emission for pristine g-C₃N₄ in (a) energy space, and (b) real space; (c) the separated e-h pairs for hydrogenated g-C₃N₄ in energy space; (d) the effectively separated e-h pairs in real space to participate the degradation processes. The charge density distribution in VBM and CBM are denoted as grey and yellow, respectively. (For interpretation of the references to colour in this figure legend, the reader is referred to the web version of this article).

(Fig. 7b), and the followed rapid recombination to emit strong PL is reasonable. On the contrary, the hydrogenation at any available atomic sites is able to cause redistribution of the charges in reciprocal space (Fig. S6b-f, S7b-f). It can be seen that the charges are also effectively separated in energy space and in real space simultaneously as shown in both Fig. 7c and d (Choosing C₂ type as a typical structure to schematically illustrate). It is of great importance to understand that this is the key factor to suppress the recombination of light induced e-h pairs. Therefore, the decrease of PL intensity can be well explained by the hydrogenation effect, and it is obviously known that the effective separated electrons and holes can effectively participate the photo-degradation process (Fig. 7d). Fig. S8 shows the electrochemical impedance spectra (EIS). It can be seen that though the two samples do not show obvious difference in conductivity at high frequency range as indicated by the inset of Fig. S8, the photocurrent density obtained on a hydrogenated g-C₃N₄ film is greatly exceeding that of as-received sample (Fig. S9). This is another evidence to indirectly reflect the effective charge separation.

The obvious enhanced absorption of the light and followed by effective spatially separation of electron-hole pairs to prevent recombination can be achieved by hydrogenation of g-C₃N₄, giving rise to the overall excellent photodegradation performance. Previously, charge separation spatially among crystal facets of the same material have obtained great attention in photocatalytic community due to the

enhanced performance [39,40]. The charge separation is because of the differences of the energy levels in the conduction bands and the valence bands between the different crystal facets. The typical instances are the {010} and {110} crystal facets of TiO₂ [39], and {010} and {110} crystal facets of BiVO₄, [40]. Most recently, it is reported that hybridizing with C_{ring} can enhance photocatalytic performance of g-C₃N₄ due to the effective spatial charge separation [41]. Thus, spatial separation of photon induced e-h pairs is essentially for enhancing photocatalytic performance. Different from the aforementioned spatial charge separation mechanism, this work reveals the local spatial charge separation effect from viewpoints of molecular structure dynamics and electronic structure evolution on the basis of modifying g-C₃N₄ structure symmetry only.

3. Conclusion

In summary, a simple one-step method for realizing effective hydrogenation of g-C₃N₄ is achieved. Molecular structure dynamics study concludes that the hydrogenation is preferred to form at 4 different sites of g-C₃N₄ to lowering the system energy. The original flat basal plane of pristine g-C₃N₄ changed to corrugated structure after hydrogenation, and the charges are spatially separated effectively as suggested by the theoretical crystal models, which is also reflected by the obvious decrease of PL intensity. This is the key factor for the dramatically

enhanced photocatalytic performance in degrading RhB molecules. The hydrogenation also shifts the bandgap larger to present blueshifted UV-vis absorption peak and PL peaks, resulting in a much better photocatalytic performance on the basis of using UV-vis light irradiation rather than the visible light irradiation only. This work not only presents a facile route to achieve exfoliation and hydrogenation of g-C₃N₄ for enhanced photocatalytic performance, but also fundamentally reveals both crystal and electronic structure evolutions induced effective charge separation for the hydrogenation of g-C₃N₄, which is of great significance for strategically guiding further exploration of more and more potential properties of g-C₃N₄ through molecular geometry modeling.

4. Experimental section

4.1. Reagents and materials

The bulk g-C₃N₄ was prepared by annealing dicyandiamide (Aladdin, China) in a quartz tube furnace at 560 °C for 6 h in air (Before reaching 560 °C, the ramping rate is set as slow as 1.56 °C/min). The bulk g-C₃N₄ (0.4 g) were mixed with 8 ml of H₂SO₄ (98 wt%) and PVP (0.5 g) in three-necked flask equipped with reflux condenser, nitrogen inlet, and temperature controller. The solution was deoxygenated by bubbling nitrogen gas at room temperature for 1 h. Finally, this mixture was kept at 50 °C and magnetically stirred for 7 h under the atmosphere of nitrogen. Then, the mixture was slowly poured into 40 mL of deionized water and sonicated for exfoliation. The temperature of the suspension increased to 120 °C rapidly, and the color changed from yellow to light yellow, after sonicated, the color turned to almost white (Fig. 2a). The final obtained suspension were separated by centrifugation and washed with an excess amount of deionized water and absolute ethanol six times to remove any impurities and unexfoliated g-C₃N₄, then dried in vacuum with the lyophilizer for 24 h.

4.2. Apparatus and measurements

Tube furnace (OTF-1200X) was used to annealing dicyandiamide in ambient air environment. The SEM images were observed by a field emission scanning electron microscope (SU-70, Hitachi High-tech Naka, JAN). The TEM images were observed by FEI Talos-F200 s. The powder X-ray diffraction (XRD) measurements were conducted on a Bruker D8-A25 X-ray diffractometer for monochromatized Cu K α (0.15406 nm) radiation. The UV-vis absorption spectra were recorded by a UV-1800 spectrophotometer (Xiamen Suo Yan technology co., LTD). The photoluminescence measurements were carried out by using a Horiba HR Evo system with excitation laser wavelength of 325 nm and 40 × UV-objective lens. The laser power is strictly controlled below 0.5 mW to avoid laser induced thermal effect on the sample. The size of the focused laser beam is ~3 μm and the pinhole is 100 for each spectrum. In order to obtain the optimized comparison of the spectra, all the spectra were collected using the same parameters. The surface chemical composition of the photocatalysts were determined by using an X-ray photoelectron spectrometer (XPS, ESCALAB 250). The photocurrent response experiment was measured with an electrochemical analyzer in a two-electrode system under zero bias. NaClO₄ (0.1 mol/L) aqueous solution was used as the electrolyte. The samples and a Pt wire work as the working electrode and the counter electrode, respectively. Electrochemical tests were conducted on a CHI760E workstation at room temperature in 0.5 M Na₂SO₄ as electrolyte. 4 mg as-received and hydrogenated g-C₃N₄ was dispersed in 330 uL and 300 uL of ethanol, respectively, and 5 uL of samples were deposited on 4 mm diameter of graphite electrode. The Ag/AgCl in saturated 3 M KCl solution and Pt plate were used as the reference electrode and the counter electrode, respectively. The electrochemical impedance spectrum (EIS) measurement was carried out with a frequency range from 100 MHz to 100 mHz at an AC amplitude of 10 mV. The photocatalytic activity measurements

were evaluated by testing the degradation of RhB and MO molecules, respectively. In each run by UV-vis irradiation and visible light irradiation (with a 400 nm cutoff), 30 mL of RhB (or MO) solution (5 ppm) containing 5 mg of photocatalysts (bulk g-C₃N₄ or acidified g-C₃N₄) were placed in a glass beaker. At certain time intervals, 2 mL of the suspensions were taken and centrifuged to remove the particles. The concentration of RhB and MO were analyzed by recording the absorption intensity resepectively at ~555 nm and ~480 nm using a UV-vis spectrophotometer.

Conflict of interest

The authors declare no competing financial interest.

Acknowledgements

This work was supported by the Natural Science Foundation of Fujian Province of China (Grant No. 2017J01005), NSFC (Grant No.11404272), the Fundamental Research Funds for the Central Universities (Grant No. 20720140514), and the Doctoral Fund of the Ministry (Grant No. 20130121110018). The work in CQU was supported by the National Key Research and Development Program of China (Grant No. 2016YFE0125200 and 2016YFC0101100). The work in NUS was supported by Singapore National Research Foundation (Grant No. NRF2017NRF-NSFC001-007). The authors acknowledge Dr. He Ren (Photocurrent measuremnt), Mr. Yange Wang (FTIR measurement), Mr. Jimming Wang (TEM measurement), and Dr. Rui Yu (XRD analysis) for their technical helps in experiments. The authors acknowledge Prof. Linfei Lai and Mr. Haimin Liu from Nanjing Tech University for the helpful discussion and measurement of EIS. The authors acknowledge Prof. Zhuofeng Hu from Sun Yat-sen University for the very useful discussion.

Appendix A. Supplementary data

Supplementary material related to this article can be found, in the online version, at doi:<https://doi.org/10.1016/j.apcatb.2019.03.001>.

References

- [1] X.B. Chen, L. Liu, P.Y. Yu, S.S. Mao, Increasing solar absorption for photocatalysis with black hydrogenated titanium dioxide nanocrystals, *Science* 331 (2011) 746–750.
- [2] L.P. Hansen, Q.M. Ramasse, C. Kisielowski, M. Brorson, E. Johnson, H. Topsøe, S. Helveg, Atomic-scale edge structures on industrial-style Mo₂ nanocatalysts, *Angewandte Chemie-Int. Ed.* 50 (2011) 10153–10156.
- [3] W.J. Ong, L.L. Tan, Y.H. Ng, S.T. Yong, S.P. Chai, Graphitic carbon nitride (g-C₃N₄)-based photocatalysts for artificial photosynthesis and environmental remediation: Are we a step closer to achieving sustainability? *Chem. Rev.* 116 (2016) 7159–7329.
- [4] T. Botari, W.P. Huhn, V.W.H. Lau, B.V. Lotsch, V. Blum, Thermodynamic equilibria in carbon nitride photocatalyst materials and conditions for the existence of graphitic carbon nitride g-C₃N₄, *Chem. Mater.* 29 (2017) 4445–4453.
- [5] Z.X. Zhou, Y.Y. Zhang, Y.F. Shen, S.Q. Liu, Y.J. Zhang, Molecular engineering of polymeric carbon nitride: advancing applications from photocatalysis to biosensing and more, *Chem. Soc. Rev.* 47 (2018) 2298–2321.
- [6] X.C. Wang, K. Maeda, A. Thomas, K. Takanabe, G. Xin, J.M. Carlsson, K. Domèn, M. Antonietti, A metal-free polymeric photocatalyst for hydrogen production from water under visible light, *Nat. Mater.* 8 (2009) 76–80.
- [7] F. Goettmann, A. Fischer, M. Antonietti, A. Thomas, Metal-free catalysis of sustainable Friedel-Crafts reactions: direct activation of benzene by carbon nitrides to avoid the use of metal chlorides and halogenated compounds, *Chem. Commun. (Camb.)* (2006) 4530–4532.
- [8] S.W. Cao, J.G. Yu, G-C₃N₄-Based photocatalysts for hydrogen generation, *J. Phys. Chem. Lett.* 5 (2014) 2101–2107.
- [9] S.C. Yan, Z.S. Li, Z.G. Zou, Photodegradation performance of g-C₃N₄ fabricated by directly heating melamine, *Langmuir* 25 (2009) 10397–10401.
- [10] S.C. Yan, Z.S. Li, Z.G. Zou, Photodegradation of rhodamine B and methyl orange over boron-doped g-C₃N₄ under visible light irradiation, *Langmuir* 26 (2010) 3894–3901.
- [11] Y.C. Bao, K.Z. Chen, Novel Z-scheme BiOBr/reduced graphene oxide/protonated g-C₃N₄ photocatalyst: synthesis, characterization, visible light photocatalytic activity and mechanism, *Appl. Surf. Sci.* 437 (2018) 51–61.

- [12] J.C. Wang, H.C. Yao, Z.Y. Fan, L. Zhang, J.S. Wang, S.Q. Zang, Z.J. Li, Indirect Z-Scheme BiOI/g-C₃N₄ photocatalysts with enhanced photoreduction CO₂ activity under visible light irradiation, *ACS Appl. Mater. Interfaces* 8 (2016) 3765–3775.
- [13] Y.C. Ye, H. Yang, X.X. Wang, W.J. Feng, Photocatalytic, Fenton and photo-Fenton degradation of RhB over Z-scheme g-C₃N₄/LaFeO₃ heterojunction photocatalysts, *Mater. Sci. Semicond. Process.* 82 (2018) 14–24.
- [14] S.X. Hua, D. Qu, L. An, W.S. Jiang, Y.J. Wen, X.Y. Wang, Z.C. Sun, Enhancing photocatalytic performance by constructing ultrafine TiO₂ nanorods/g-C₃N₄ nanosheets heterojunction for water treatment, *Appl. Catal. B* 240 (2019) 253–261.
- [15] F. Dong, Z.W. Zhao, T. Xiong, Z.L. Ni, W.D. Zhang, Y.J. Sun, W.K. Ho, In situ construction of g-C₃N₄/g-C₃N₄ metal-free heterojunction for enhanced visible-light photocatalysis, *ACS Appl. Mater. Interfaces* 5 (2013) 11392–11401.
- [16] Z.J. Li, Y.C. Xing, X.Y. Fan, L.G. Lin, A. Meng, Q.D. Li, rGO/protonated g-C₃N₄ hybrid membranes fabricated by photocatalytic reduction for the enhanced water desalination, *Desalination* 443 (2018) 130–136.
- [17] X.R. Du, G.J. Zou, Z.H. Wang, X.L. Wang, A scalable chemical route to soluble acidified graphitic carbon nitride: an ideal precursor for isolated ultrathin g-C₃N₄ nanosheets, *Nanoscale* 7 (2015) 8701–8706.
- [18] T.Y. Ma, Y.H. Tang, S. Dai, S.Z. Qiao, Proton-functionalized two-dimensional graphitic carbon nitride nanosheet: an excellent metal-/label-free biosensing platform, *Small* 10 (2014) 2382–2389.
- [19] Z.X. Zhou, J.H. Wang, J.C. Yu, Y.F. Shen, Y. Li, A.R. Liu, S.Q. Liu, Y.J. Zhang, Dissolution and liquid crystals phase of 2D polymeric carbon nitride, *J. Am. Chem. Soc.* 137 (2015) 2179–2182.
- [20] Q. Li, D. Xu, J.N. Guo, X. Ou, F. Yan, Protonated g-C₃N₄@polypyrrole derived N-doped porous carbon for supercapacitors and oxygen electrocatalysis, *Carbon* 124 (2017) 599–610.
- [21] F.X. Cheng, H.N. Wang, X.P. Dong, The amphoteric properties of g-C₃N₄ nanosheets and fabrication of their relevant heterostructure photocatalysts by an electrostatic re-assembly route, *Chem. Commun.* 51 (2015) 7176–7179.
- [22] W.J. Ong, L.K. Putri, Y.C. Tan, L.L. Tan, N. Li, Y.H. Ng, X.M. Wen, S.P. Chai, Unravelling charge carrier dynamics in protonated g-C₃N₄ interfaced with carbon nanodots as co-catalysts toward enhanced photocatalytic CO₂ reduction: a combined experimental and first-principles DFT study, *Nano Res.* 10 (2017) 1673–1696.
- [23] J. Xu, L.W. Zhang, R. Shi, Y.F. Zhu, Chemical exfoliation of graphitic carbon nitride for efficient heterogeneous photocatalysis, *J. Mater. Chem. A Mater. Energy Sustain.* 1 (2013) 14766–14772.
- [24] B.V. Lotsch, M. Doblinger, J. Sehnert, L. Seyfarth, J. Senker, O. Oeckler, W. Schnick, Unmasking melon by a complementary approach employing electron diffraction, solid-state NMR spectroscopy, and theoretical calculations-structural characterization of a carbon nitride polymer, *Chem. Eur. J.* 13 (2007) 4969–4980.
- [25] X.Y. Yuan, C. Zhou, Y.R. Jin, Q.Y. Jing, Y.L. Yang, X. Shen, Q. Tang, Y.H. Mu, A.K. Du, Facile synthesis of 3D porous thermally exfoliated g-C₃N₄ nanosheet with enhanced photocatalytic degradation of organic dye, *J. Colloid Interface Sci.* 468 (2016) 211–219.
- [26] Z. Chen, T.T. Fan, M.Y. Shao, X. Yu, Q.L. Wu, J.H. Li, W.P. Fang, X.D. Yi, Simultaneously enhanced photon absorption and charge transport on a distorted graphitic carbon nitride toward visible light photocatalytic activity, *Appl. Catal. B-Environ.* 242 (2019) 40–50.
- [27] J.S. Zhang, M.W. Zhang, L.H. Lin, X.C. Wang, Sol processing of conjugated carbon nitride powders for thin-film fabrication, *Angewandte Chemie-Int. Ed.* 54 (2015) 6297–6301.
- [28] S.W. Zhang, J.X. Li, X.K. Wang, Y.S. Huang, M. Zeng, J.Z. Xu, In situ ion exchange synthesis of strongly coupled Ag@AgCl/g-C₃N₄ porous nanosheets as plasmonic photocatalyst for highly efficient visible-light photocatalysis, *ACS Appl. Mater. Interfaces* 6 (2014) 22116–22125.
- [29] X.J. Bai, L. Wang, R.L. Zong, Y.F. Zhu, Photocatalytic activity enhanced via g-C₃N₄ nanoplates to nanorods, *J. Phys. Chem. C* 117 (2013) 9952–9961.
- [30] P. Ruffieux, O. Groning, P. Schwaller, L. Schlapbach, P. Groning, Hydrogen atoms cause long-range electronic effects on graphite, *Phys. Rev. Lett.* 84 (2000) 4910–4913.
- [31] P. Niu, M. Qiao, Y.F. Li, L. Huang, T.Y. Zhai, Distinctive defects engineering in graphitic carbon nitride for greatly extended visible light photocatalytic hydrogen evolution, *Nano Energy* 44 (2018) 73–81.
- [32] Y.J. Zhang, M. Antonietti, Photocurrent generation by polymeric carbon nitride solids: an initial step towards a novel photovoltaic system, *Chem. Asian J.* 5 (2010) 1307–1311.
- [33] P. Niu, L.L. Zhang, G. Liu, H.M. Cheng, Graphene-like carbon nitride nanosheets for improved photocatalytic activities, *Adv. Funct. Mater.* 22 (2012) 4763–4770.
- [34] R.Y. Zhang, M.Z. Ma, Q. Zhang, F. Dong, Y. Zhou, Multifunctional g-C₃N₄/graphene oxide wrapped sponge monoliths as highly efficient adsorbent and photocatalyst, *Appl. Catal. B-Environ.* 235 (2018) 17–25.
- [35] T. Xiong, W.L. Cen, Y.X. Zhang, F. Dong, Bridging the g-C₃N₄ interlayers for enhanced photocatalysis, *ACS Catal.* 6 (2016) 2462–2472.
- [36] F.X. Cheng, J. Yan, C.J. Zhou, B.H. Chen, P.R. Li, Z. Chen, X.P. Dong, An alkali treating strategy for the colloidization of graphitic carbon nitride and its excellent photocatalytic performance, *J. Colloid Interface Sci.* 468 (2016) 103–109.
- [37] Q. Zhang, S.Z. Liu, Y.C. Zhang, A.P. Zhu, J. Li, X.H. Du, Enhancement of the photocatalytic activity of g-C₃N₄ via treatment in dilute NaOH aqueous solution, *Mater. Lett.* 171 (2016) 79–82.
- [38] J. Yan, Z.G. Chen, H.Y. Ji, Z. Liu, X. Wang, Y.G. Xu, X.J. She, L.Y. Huang, L. Xu, H. Xu, H.M. Li, Construction of a 2D graphene-like MoS₂/C₃N₄ heterojunction with enhanced visible-light photocatalytic activity and photoelectrochemical activity, *Chem. Eur. J.* 22 (2016) 4764–4773.
- [39] J. Pan, G. Liu, G.M. Lu, H.M. Cheng, On the true photoreactivity order of {001}, {010}, and {101} facets of anatase TiO₂ crystals, *Angewandte Chemie-Int. Ed.* 50 (2011) 2133–2137.
- [40] R.G. Li, F.X. Zhang, D.G. Wang, J.X. Yang, M.R. Li, J. Zhu, X. Zhou, H.X. Han, C. Li, Spatial separation of photogenerated electrons and holes among {010} and {110} crystal facets of BiVO₄, *Nat. Commun.* 4 (2013) 1432.
- [41] W. Che, W.R. Cheng, T. Yao, F.M. Tang, W. Liu, H. Su, Y.Y. Huang, Q.H. Liu, J.K. Liu, F.C. Hu, Z.Y. Pan, Z.H. Sun, S.Q. Wei, Fast photoelectron transfer in (C-ring)-C₃N₄ plane heterostructural nanosheets for overall water splitting, *J. Am. Chem. Soc.* 139 (2017) 3021–3026.